Dependence of accessible dark matter annihilation cross sections on the density profiles of dwarf spheroidal galaxies with the Cherenkov Telescope Array

Nagisa Hiroshima,[1,2,3] Masaaki Hayashida,[4] and Kazunori Kohri[3,5,6]

[1]*RIKEN Interdisciplinary Theoretical and Mathematical Sciences (iTHEMS), Wako, Saitama 351-0198, Japan*
[2]*Institute for Cosmic Ray Research, The University of Tokyo, Kashiwa, Chiba 277-8582, Japan*
[3]*Institute of Particle and Nuclear Studies, KEK, Tsukuba, Ibaraki 305-0801, Japan*
[4]*Department of Physics, Faculty of Science and Engineering, Konan University, 8-9-1 Okamoto, Kobe, Hyogo 658-8501, Japan*
[5]*The Graduate University for Advanced Studies (SOKENDAI), Tsukuba, Ibaraki 305-0801, Japan*
[6]*Rudolf Peierls Centre for Theoretical Physics, The University of Oxford, Parks Road, Oxford OX1 3PU, United Kingdom*

(Received 16 March 2019; published 21 June 2019)

Dwarf spheroidal galaxies are excellent targets in γ-ray searches for dark matter. We consider dark matter searches in dwarf spheroidal galaxies (dSphs) with the Cherenkov Telescope Array (CTA). The aim of this work is to reveal a quantitative and precise dependence of the accessible dark matter annihilation cross sections on the dark matter density profiles of dSphs and on the distance to them. In most data analyses, researchers have assumed pointlike signals from dSphs because it is difficult to resolve the expected emission profiles with current γ-ray observatories. In future however, CTA will be able to resolve the peak emission profiles in dSphs. We take several variations of the dark matter density profile of Draco dSph as examples and analyze the simulated observations of with CTA. We derive the accessible region of the dark matter annihilation cross-section with each dark matter density profile. The accessible region of the annihilation cross section can differ by a factor of 10 among plausible profiles. We also examine the dependence on the distance to the target dSphs by assuming the same profiles of dSphs at different distances. Closer targets are better due to the higher J-factor, while their spatial extension significantly degrades our reach to the annihilation cross section compared to the value expected from a simple distance scaling of the J-factor. Spatial extension of the source affects the probable parameter region in energy-dependent ways. In some γ-ray energy ranges, this behavior becomes moderately dependent on the properties of the observation facility.

DOI: 10.1103/PhysRevD.99.123017

I. INTRODUCTION

Dark matter (DM) is a massive and invisible matter component of the Universe [1–3]. Rotation curves of galaxies [4–7] and bullet cluster–like encounters [8,9] are examples that indicate the existence of DM. Standard cosmology also requires DM, since nonrelativistic matter components different from baryons are necessary to form structures of the Universe [10,11]. Cosmological observations indicate that DM occupies approximately a quarter of the total energy in the Universe [11–14].

Varieties of candidates for DM are proposed. One possibility is that DM is a new particle: weakly interacting massive particles (WIMPs) (see, e.g., Refs. [15,16]), strongly interacting massive particles (see, e.g., Refs. [17,18]), axions (see, e.g., Refs. [19–21]), or sterile neutrinos (see, e.g., Refs. [22–25]) are examples. Nonparticle solutions like primordial black holes (see, e.g., Refs. [26–30]) are also considered. In this paper, we focus on DM categorized as WIMPs. WIMPs are one of the best-studied candidates proposed in theories beyond the standard model like supersymmetric extensions (see, e.g., Refs. [31–35]). For WIMPs to be DM particles that explain nonrelativistic, electromagnetically neutral, invisible components in Refs. [11,13], their mass must be around $m_{\rm DM} \sim \mathcal{O}(\mathrm{GeV})$ to $\mathcal{O}(\mathrm{TeV})$, and they must have a velocity-averaged freeze-out annihilation cross section $\langle \sigma v \rangle \sim 3 \times 10^{-26}\ \mathrm{cm}^3/\mathrm{s}$ [36]. This value of the cross section is referred to as the canonical cross section.

WIMPs as DM can be detectable through their feeble interaction with standard model particles. Three kinds of strategies are pursued: productions of DM with colliders (see, e.g., Refs. [37,38]); measuring the scattering between DM particles and nuclei (see, e.g., Refs. [39–41]), called direct detection experiments; and the search for standard model particles produced after DM self-annihilation in the

Universe, called indirect detection experiments. There has been no confirmed detection of particle DM nor DM yet. For WIMP models of $m_{\rm DM} \sim \mathcal{O}(1\text{–}10)$ GeV, γ-ray observations already constrain the DM annihilation cross section to be smaller than the canonical value [42]. Lighter DM is constrained from structure formation (see, e.g., Refs. [43–46]). WIMPs heavier than $m_{\rm DM} \sim \mathcal{O}(10)$ GeV are less constrained and expected to be discovered or excluded in ongoing and future experiments.

Indirect detection experiments have advantages in DM searches at higher energy ranges of $m_{\rm DM} \gtrsim \mathcal{O}(1)$ TeV. Techniques for astrophysical observations to detect high-energy emissions are already developed [47–51]. A plethora of projects searching DM signals in the Universe with charged cosmic rays (see, e.g., Refs. [52–54]), neutrinos (see, e.g., Refs. [55,56]), and γ-rays are ongoing. In general, astrophysical emissions dominate over DM signals, and elaborate strategies are required in the indirect DM search. Spectral and morphological information of emissions helps identify the sources. Considering DM searches in γ-rays with a facility of threshold energy $E_{\rm th}$, the flux from DM annihilations is

$$\phi = \frac{1}{4\pi}\frac{\langle \sigma v \rangle}{2m_{\rm DM}^2}\int_{E_{\rm th}}^{m_{\rm DM}} dE \frac{dN_\gamma}{dE} \cdot J, \tag{1}$$

where

$$J = \int d\Omega \frac{dJ}{d\Omega} = \int d\Omega \int ds \rho_{\rm DM}^2. \tag{2}$$

In Eq. (1), all quantities except for J are determined from particle physics. The part shown as J in Eq. (2) is referred to as the "(astrophysical) J-factor." Since the J-factor is defined as the line-of-sight integral over the squared DM density $\rho_{\rm DM}^2$, the signal sensibly depends on the density profile, and precise information about the DM distribution at the source is necessary to reliably derive the WIMP properties. The distribution of the DM is determined from stellar kinematics in optical observations (see, e.g., Ref. [57]).

The Galactic center is considered one of the best targets to search DM signals in γ-rays (see, e.g., Ref. [58]) because it is expected to have the highest J-factor among known targets with $J \sim \mathcal{O}(10^{21\text{–}22})$ GeV^2 cm^{-5}. Attentive strategies in the separation of DM signals from astrophysical emissions are required since the Galactic center is very bright in astrophysical γ-ray emissions [59]. Also, the determination of the precise shape and a normalization of the DM density distribution at the very center of the Milky Way Galaxy are remaining issues [60–63]. Dwarf spheroidal galaxies (dSphs) are satellites of the Milky Way Galaxy and also good regions to focus on as first pointed out by Ref. [64] and later in Ref. [65]. They are spatially extended objects of $\mathcal{O}(1)$ degrees located in high-latitude regions of the Milky Way galaxy. Several tens of dSphs are already identified with available stellar kinematics data, and the number of confirmed dSphs is continuously increasing [66–75]. Stellar motions in dSphs indicate that they are dense and DM dominated objects [76–78] with mass-to-luminosity ratios reaching approximately $10^3\ M_\odot/L_\odot$ [79–83]. No significant γ-ray emissions have been confirmed in dSphs, although possibilities that some of them contain γ-ray sources cannot be excluded [42,84].

Stacking analyses on dSphs by the Fermi collaborations give the tightest upper limits on DM annihilation cross sections [42,85–89]. For DM of $m_{\rm DM} \lesssim \mathcal{O}(100)$ GeV, the upper limits already reach the canonical value [42,85–89]. At higher mass ranges, ground-based Cherenkov telescopes have advantages over observations with satellite detectors. Since most of those ground-based γ-ray facilities are pointing telescopes, upper limits on DM annihilation cross sections are obtained by observations on a few well-selected dSphs. Almost the same level of upper limits is obtained by observations with different facilities [90–103]. In the very near future, the Cherenkov Telescope Array (CTA) will start its operations and is expected to improve the sensitivity to probe DM annihilation cross sections by about 1 order of magnitude [51].

The designed angular resolution of CTA for γ-rays around 1 TeV is $\mathcal{O}(0.05°)$, which is finer than the typical spatial extension of dSphs, and hence the consideration of the DM density profile shape becomes crucial. This has been pointed out in earlier works (see, e.g., Refs. [77,104]). In the latest analyses with atmospheric Cherenkov telescopes, spatial extensions of DM for dSphs are taken into account [93,100] and tend to give upper limits milder than those assuming point sources. However, DM density distributions in the dSphs are still under discussion (see the Appendix of Ref. [77] or Ref. [105] for examples). Different models for DM distributions lead to the divergence of derived upper limits.

In this paper, we examine accessible parameter regions of the DM annihilation cross section with CTA, probing different extended DM density distributions in dSphs. We sample DM density profiles of the Draco dSph as examples. Draco is one of the well-known classical dSph galaxies. So far, several profiles have been provided for it in the literature [76,98,106–110]. We consider the observation of dSphs with CTA and analyze simulated data using CTOOLS [111]. The sensitivity calculations for DM annihilation cross sections are conducted with 16 different profiles and compared to give a quantitative estimate of uncertainties in the searches towards dSphs. The dependence on the distances to dSphs is also investigated.

The structure of this paper is as follows. Section II explains our methods. In Sec. III, we show a comparison of the sensitivity for annihilation cross sections obtained with various profiles and distances. Section IV is devoted to discussions. We summarize in Sec. V.

II. METHODS

A. Dark matter density profiles of the source

A point source is the simplest model for a target dSph when the angular size of the target is small enough compared to the angular resolution of observational facilities. Future ground-based atmospheric Cherenkov telescopes can resolve typical dSphs, so they are to be treated as extended sources. Profiles of dSphs are sampled to investigate how their spatial extension affects the accessible region of the DM annihilation cross section. Draco dSph is taken as the example, and we limit our analyses to spherical profiles for simplicity. Three types of DM density profiles are considered in this work:

(1) generalized Navarro-Frenk-White (NFW) profile [112,113],

$$\rho(r) = \rho_s \left(\frac{r}{r_s}\right)^{-\gamma} \left(1 + \left(\frac{r}{r_s}\right)^{\alpha}\right)^{-\frac{\beta-\gamma}{\alpha}}, \quad (3)$$

where $(\alpha, \beta, \gamma) = (1, 3, 1)$ corresponds to the original NFW profile in Ref. [114];

(2) Burkert profile [115]:

$$\rho(r) = \rho_s \left(1 + \frac{r}{r_s}\right)^{-1} \left(1 + \left(\frac{r}{r_s}\right)^{2}\right)^{-1}; \quad (4)$$

(3) power-law (PL) profile with an exponential cutoff:

$$\rho(r) = \rho_s \left(\frac{r}{r_s}\right)^{-\alpha} \exp\left[-\frac{r}{r_s}\right]. \quad (5)$$

ρ_s is the normalization of the DM density, and r_s is the scale radius of the profile measuring the distance r from the center of the target. More detailed profiles such as nonspherical cases or profiles with substructures are discussed in Refs. [78,116–118]. Table I summarizes our reference profiles with explicit expressions of each profile, profile type [corresponding to Eqs. (3), (4), and (5)], J-factor integrated to solid angle of 0.5° ($J_{<0.5^\circ}$), J-factor integrated to the 4.0° × 4.0° region ($J_{\rm tot}$) which corresponds to the size of the region of interest (RoI) in our analyses, and distance from the Earth. We also assign identification numbers in the first column in Table I for convenience. Note that the truncation radius for the profiles is not introduced in our analyses. The truncation radius is usually determined by the location of the outermost member star or the virial radius of the DM halo. If we take the former for the truncation radius, then it corresponds to $\theta = 1.3^\circ$ for Draco [108]. On the other hand, the virial radius is highly model dependent. Actual radial extension of the dSphs is still under discussion. We chose our RoI to cover the outermost member star, avoiding the introduction of an additional model parameter.

TABLE I. DM density profiles for dSphs used in our analysis. We assign numbers in the first column for convenience. We adopt the center value for the parameters in each case.

No.	Reference	Expression	Type	$\log_{10}J_{<0.5^\circ}$	$\log_{10}J_{\rm tot}$	Distance (kpc)
1	Acciari *et al.* [98]	$(\frac{1.7\ \mathrm{GeV}}{\mathrm{cm}^3})(\frac{r}{0.79\ \mathrm{kpc}})^{-1}(1+\frac{r}{0.79\ \mathrm{kpc}})^{-2}$	NFW	18.40	18.45	80
2	Geringer-Sameth *et al.* [108]	$(\frac{0.69\ \mathrm{GeV}}{\mathrm{cm}^3})(\frac{r}{3.7\ \mathrm{kpc}})^{-0.71}(1+(\frac{r}{3.7\ \mathrm{kpc}})^{2.01})^{-2.80}$	Generalized NFW	19.00	19.44	76
3	Lokas [109]	$(\frac{16.3\ \mathrm{GeV}}{\mathrm{cm}^3})(1+\frac{r}{0.67\ \mathrm{kpc}})^{-3}$	Generalized NFW	19.08	19.29	
4		$(\frac{1.23\ \mathrm{GeV}}{\mathrm{cm}^3})(\frac{r}{1.30\ \mathrm{kpc}})^{-1}(1+\frac{r}{1.30\ \mathrm{kpc}})^{-2}$	NFW	18.80	18.91	72
5		$(\frac{0.18\ \mathrm{GeV}}{\mathrm{cm}^3})(\frac{r}{1.99\ \mathrm{kpc}})^{-1.5}(1+\frac{r}{1.99\ \mathrm{kpc}})^{-1.5}$	Generalized NFW	18.88	18.90	
6	Lokas *et al.* [110]	$(\frac{5.9\ \mathrm{GeV}}{\mathrm{cm}^3})(\frac{r}{0.32\ \mathrm{kpc}})^{-1}\exp[-\frac{r}{0.32\ \mathrm{kpc}}]$	PL + cutoff	18.53	18.53	80
7	Mashchenko *et al.* [106]	$(\frac{4.76\ \mathrm{GeV}}{\mathrm{cm}^3})(1+\frac{r}{1.41\ \mathrm{kpc}})^{-1}(1+(\frac{r}{1.41\ \mathrm{kpc}})^{2})^{-1}$	Burkert	19.08	19.56	
8		$(\frac{13.4\ \mathrm{GeV}}{\mathrm{cm}^3})(1+\frac{r}{0.35\ \mathrm{kpc}})^{-1}(1+(\frac{r}{0.35\ \mathrm{kpc}})^{2})^{-1}$	Burkert	18.65	18.70	
9		$(\frac{37.8\ \mathrm{GeV}}{\mathrm{cm}^3})(1+\frac{r}{0.18\ \mathrm{kpc}})^{-1}(1+(\frac{r}{0.18\ \mathrm{kpc}})^{2})^{-1}$	Burkert	18.69	18.70	
10		$(\frac{0.60\ \mathrm{GeV}}{\mathrm{cm}^3})(\frac{r}{2.82\ \mathrm{kpc}})^{-1}(1+\frac{r}{2.82\ \mathrm{kpc}})^{-2}$	NFW	18.95	19.15	82
11		$(\frac{1.70\ \mathrm{GeV}}{\mathrm{cm}^3})(\frac{r}{1.00\ \mathrm{kpc}})^{-1}(1+\frac{r}{1.00\ \mathrm{kpc}})^{-2}$	NFW	18.67	18.73	
12		$(\frac{4.76\ \mathrm{GeV}}{\mathrm{cm}^3})(\frac{r}{0.50\ \mathrm{kpc}})^{-1}(1+\frac{r}{0.50\ \mathrm{kpc}})^{-2}$	NFW	18.70	18.72	
13		$(\frac{13.4\ \mathrm{GeV}}{\mathrm{cm}^3})(\frac{r}{0.25\ \mathrm{kpc}})^{-1}(1+\frac{r}{0.25\ \mathrm{kpc}})^{-2}$	NFW	18.70	18.70	
14		$(\frac{37.8\ \mathrm{GeV}}{\mathrm{cm}^3})(\frac{r}{0.18\ \mathrm{kpc}})^{-1}(1+\frac{r}{0.18\ \mathrm{kpc}})^{-2}$	NFW	19.15	19.15	
15	Sanchez-Conde *et al.* [107]	$(\frac{0.95\ \mathrm{GeV}}{\mathrm{cm}^3})(\frac{r}{1.19\ \mathrm{kpc}})^{-1}\exp[-\frac{r}{1.19\ \mathrm{kpc}}]$	PL + cutoff	18.58	18.69	80
16		$(\frac{12.7\ \mathrm{GeV}}{\mathrm{cm}^3})\exp[-\frac{r}{0.24\ \mathrm{kpc}}]$	PL + cutoff	18.56	18.58	

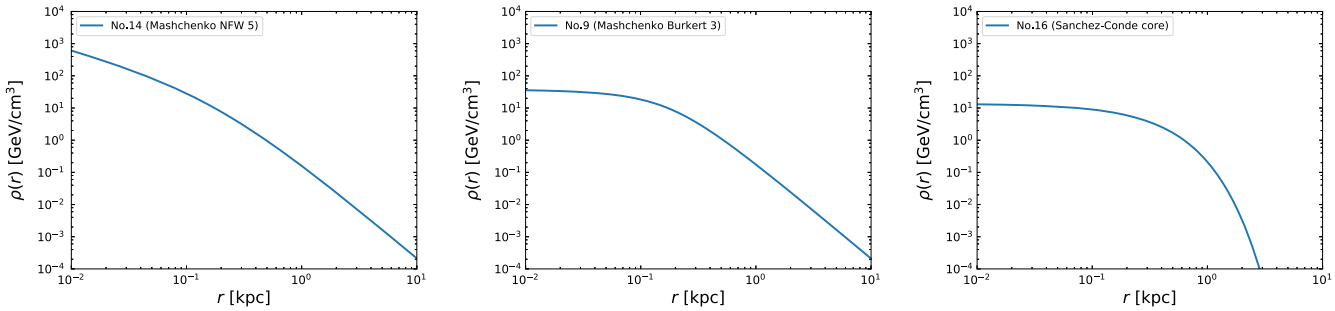

FIG. 1. Examples of DM density profiles in our analyses. *Left*: NFW profile of model 5 in Ref. [106]. *Center*: Burkert profile of model 3 in Ref. [106]. *Right*: power-law of (index 0) + cutoff profile in Ref. [107]. The horizontal axis represents the distance measured from the center of the dSph. Numbers in the legends correspond to those in Table I.

The J-factor integrated to 1.3° and $J_{\rm tot}$ defined as J-factors in our RoI differ by at most 10%. Templates of the J-factor centered on the target are generated by adopting the median value of the parameters for each profile provided in the references. The spatial resolution of our template is 0.01°. In practice, we produce templates larger than the RoI, then use parts corresponding to the RoI. $J_{<0.5^\circ}$ values in Table I are shown just to make a comparison with previous works easier and are not used in our analyses.

B. Spectrum of the DM annihilation at the source

Three channels are considered as final states, $\bar{b}b$, W^+W^-, and $\tau^+\tau^-$. Those are representatives of DM annihilations into quarks, weak bosons, and leptons. The maximum mass of the DM particle in our calculation is set to $m_{\rm DM} = 1$ PeV, while the minimum is set to $m_{\rm DM} =$ 25 GeV for lepton and quark channels and to $m_{\rm DM} =$ 160 GeV for the weak boson channel. At lower energies, contributions from residual cosmic rays are significant. We set our minimum mass to avoid these contaminations. The spectra of each annihilation channel are calculated with PYTHIA8.2 [119–121]. Figure 2 shows examples of spectra from $m_{\rm DM} = 100$ GeV to 1 PeV. The spectra shown in Fig. 2 include final state radiations like bremsstrahlung of charged leptons, which are electroweak corrections different from interactions with external fields. We consider contributions from secondary γ-rays produced during propagations of charged leptons to be negligible [122–126]. The treatment of the secondary γ-rays and the spectra in our calculation would be consistent with those available in Ref. [127], which are computed by the old version PYTHIA8.1 and widely used in γ-ray searches of dark matter.

The differences in the gamma-ray spectra between W^+W^- (or $\bar{b}b$) and $\tau^+\tau^-$ modes come from differences of the particle multiplicity among those modes. γ-rays are produced mainly by decaying neutral pions and partly by other decaying mesons. In the W^+W^- or $\bar{b}b$ modes, emitted quark pairs immediately fragment into a lot of mesons and baryons, which are dominant modes. The number of the multiplicity into pions would be approximately 30 for the center-of-momentum energy being $\sqrt{s} = {\rm O}(1)$ TeV. In this case, the γ-ray spectrum becomes broader with its mean energy being lower. On the other hand, in the $\tau^+\tau^-$ mode, the number of the multiplicity into neutral pions is much smaller [a few in $\sqrt{s} = {\rm O}(1)$ TeV]. In this latter case, the energy of γ-rays tends to be higher, which gives a steeper spectrum than that of the W^+W^- or $\bar{b}b$ emission mode.

C. General procedures of our analysis

The procedure for sensitivity calculations is as follows. The software package CTOOLS [111] is used for the

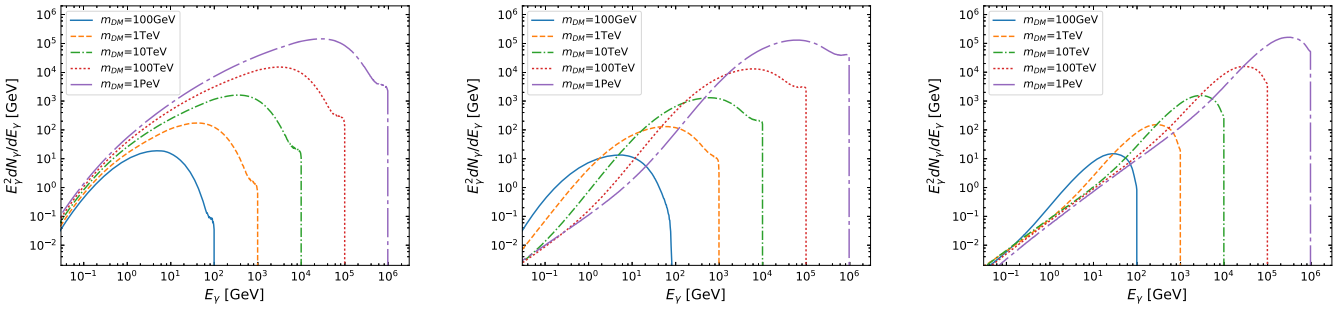

FIG. 2. γ-ray spectrum for DM of mass $m_{\rm DM} = 100$ GeV, 1 TeV, 10 TeV, 100 TeV, and 1 PeV annihilating into $\bar{b}b$ (*left*), W^+W^- (*center*), and $\tau^+\tau^-$ (*right*). Spectrum of $m_{\rm DM} = 100$ GeV annihilating into W^+W^- is shown for comparison and not used in our analyses.

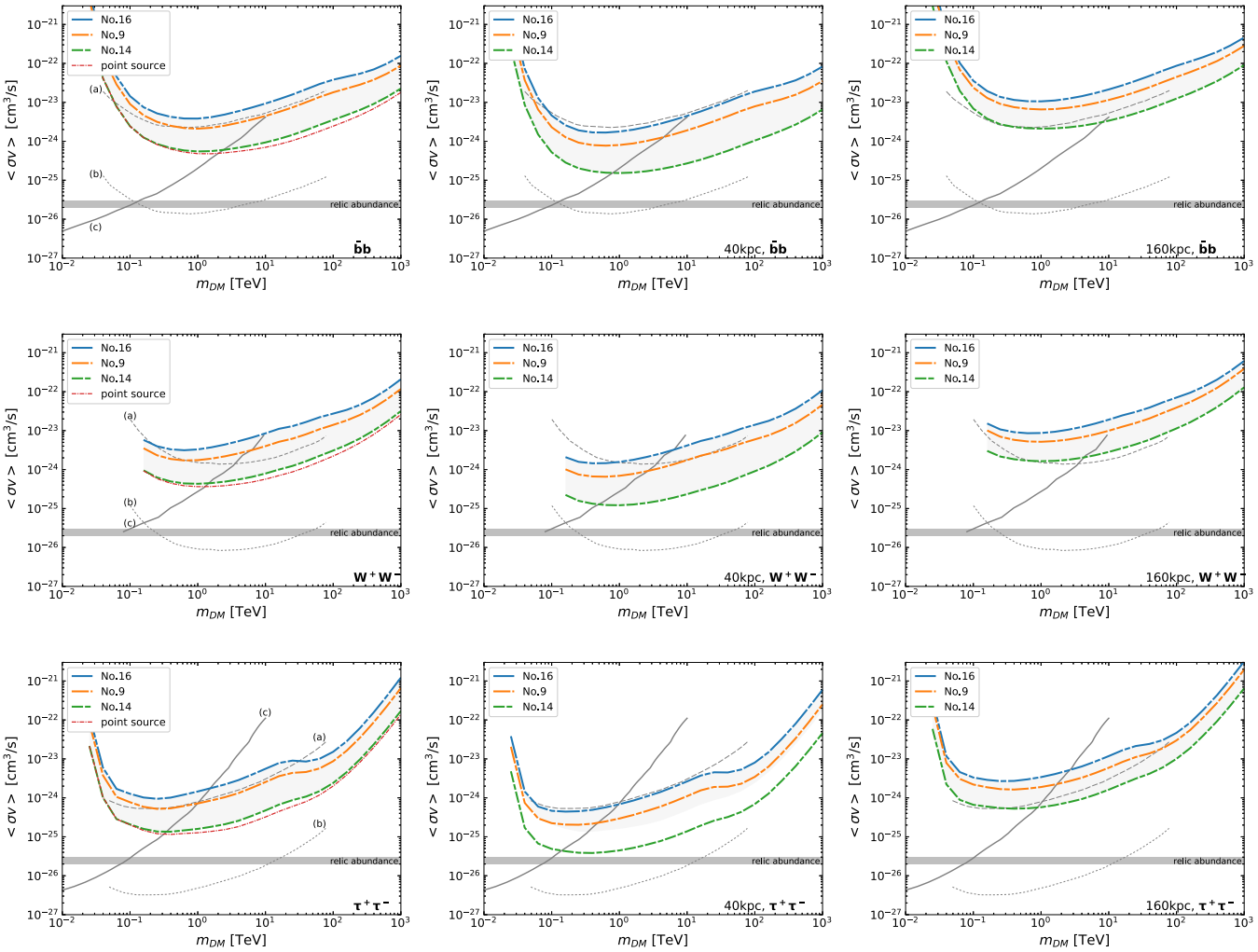

FIG. 3. Upper limits on the DM annihilation cross section assuming a 500 hr observation. In each panel, we show our results with dash-dotted lines using several dash lengths. For comparison, we put three lines: (a) the CTA sensitivity curve for a 500 hr observation of the Galactic halo with CTA [51] assuming a Burkert profile (long-dashed line), (b) the same but assuming an Einasto profile (short-dashed line), and (c) an observational result of the current upper limit by Fermi-LAT using 25 dSphs with kinematically derived J-factors [88] (solid line). We also show a reference for the cross section $\langle \sigma v \rangle$ corresponding to the relic abundance in a horizontal band in the bottom part. Detailed calculations for the relic abundance is given in, e.g., Ref. [36]. Panels in the left column show sensitivities assuming profiles in Table I. The distance for each profile is also shown in the same table. The severest case of $J_{\rm tot} = 10^{19.15}$ (number 14 in Table I, left panel in Fig. 1) is shown with a short dashed-dotted line, and the weakest one of $J_{\rm tot} = 10^{18.58}$ (number 16 in Table I, right panel in Fig. 1) is shown with a long dash-dotted line. Middle dash-dotted lines correspond to the case of the center panel in Fig. 1 of $J_{\rm tot} = 10^{18.70}$ (number 9). We also show the upper limits, assuming a point source of $J_{\rm tot} = 10^{19.15}$ with the shortest dash-dotted lines. The center (right) column shows the achievable sensitivities assuming the same profiles of the 16 sources in Table I at 40 kpc (160 kpc) from the Earth. In each column, the top, middle, and bottom panels correspond to the upper limits on annihilation cross sections of DM into $\bar{b}b$, W^+W^-, and $\tau^+\tau^-$, respectively.

analysis. First, we simulate events assuming a 500 hr observation. The instrumental response function (IRF) PROD3B [128], the latest publicly available version of the CTA IRF package, is used. Assuming the northern CTA site (La Palma), we select the IRF optimized for the long-time observation at a zenith angle of 20°. In the event generations, no γ-ray sources are included. Only residual charged cosmic rays as background events are simulated. After the event generation, selections and binnings are performed in energy and space. We select a $4° \times 4°$ square region centered on the target. Spatial binning is 0.03°. In energy, events from 0.03 to 180 TeV are selected and binned with five bins per decade on a logarithmic scale. We conduct likelihood analyses with the binned data. Median upper limits on the γ-ray flux are defined to decrease the likelihood corresponding to a 95% confidence level. Throughout the procedure, we calculate with CTOOLS, following the method in Ref. [111]. The dependence between the γ-ray flux and annihilation cross section is given in Eq. (1).

III. RESULTS

We conduct likelihood analyses on the simulated 500 hr observation of a dSph with DM density profiles listed in Table I. The top, middle, and bottom rows in Fig. 3 show the cases of DM annihilating into $\bar{b}b$, W^+W^-, and $\tau^+\tau^-$, respectively. Panels in the left column show the sensitivities, assuming the DM density profiles, distances, and J-factors ($J_{\rm tot}$) in Table I. Each line is the 95% level upper limit corresponding to the profile in Fig. 1. Upper limits assuming profile number 14 (NFW model 5 in Ref. [106]) are the strongest, while number 16 (PL of

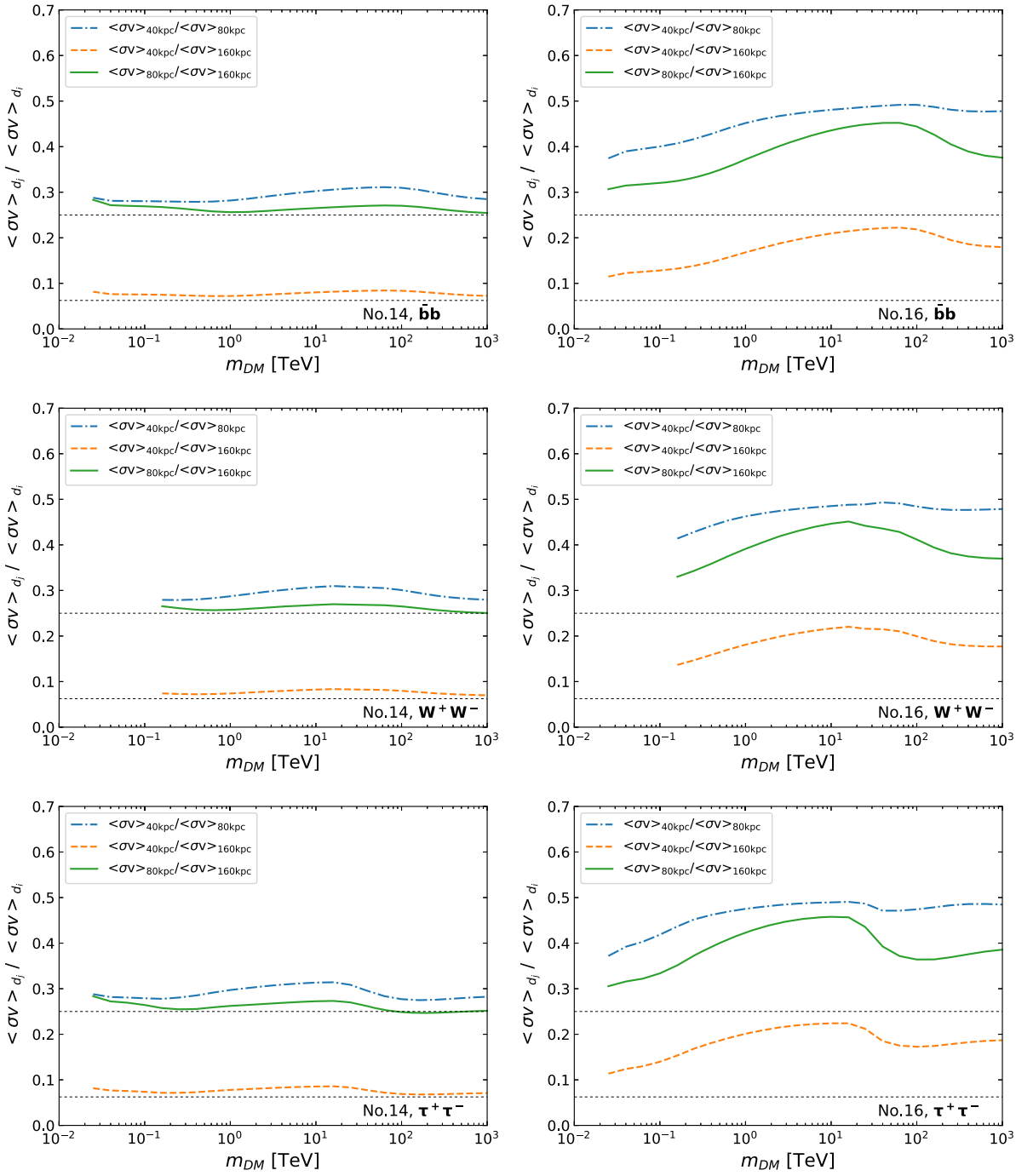

FIG. 4. The ratio between the upper limits on the annihilation cross section, assuming the same profiles of dSphs at different distances, considering profile number 14 (left) and number 16 (right). The expected value of ratios $\langle\sigma v\rangle_{d_j}/\langle\sigma v\rangle_{d_i}$ from the difference of J-factors are shown as dotted lines. The ratio of $(1/2)^2$ are expected for $(d_j, d_i) = (40\ \text{kpc}, 80\ \text{kpc})$ and (80 kpc, 160 kpc), while $(1/4)^2$ is expected for $(d_j, d_i) = (40\ \text{kpc}, 160\ \text{kpc})$. Deviations from the scaling from the J-factor are higher for the case of profile number 16.

index 0 + cutoff model in Ref. [107]) is the weakest in our sample. Other profiles give the upper limits in the shaded regions of the Fig. 3, like middle-dash dotted lines corresponding to the cases of number 9. Sensitivities with a point source of $\log_{10}(J) = 19.15$, which is the same as the J-factor of profile number 14, are also shown in a thin dash-dotted line. If we assume a point source, the upper limit always gets stronger. With the angular resolution of CTA, extended source structures are clearly resolved. Our results are consistent with the analytical discussion in Ref. [104]. Comparing between annihilation channels, wider regions of the cross section parameter space can be covered for DM annihilating into $\tau^+\tau^-$ than for $\bar{b}b$ or W^+W^- channels. This is due to the hard spectral feature which can be seen in the right panel of the Fig. 2. The tendency is consistent with the latest results in Ref. [129], which assumes line + broad spectra in specific WIMP models. Features in the sensitivity curves in Fig. 3 at $m_{\rm DM} = \mathcal{O}(10)$–$\mathcal{O}(100)$ TeV result from the properties of the telescope. Center (right) columns show the sensitivities for sources at smaller (larger) distances. We adopt the same distance among the profiles here. Differences between profiles are larger (smaller) for cases assuming 40 (160) kpc due to the angular extensions. In each panel, we also show the current limit by Fermi using 25 dSphs [88] with a solid line and the expected sensitivities of the Galactic halo observations using CTA with dashed lines [51,61,130–132]. We show two cases, assuming different DM density profiles for the expectations of Galactic halo. observations because the DM density profile there is under discussion. The accessible annihilation cross section is about 2 orders of magnitude smaller for the case assuming the Einasto profile (short-dashed line) than that assuming the Burkert profile (long-dashed line) as shown in these figures.

We can expect better constraints when we adopt profiles based on the latest and detailed modelings of the dSphs. For example, we do not include the contribution from subhalos in dSphs since it is still under discussion (e.g., Refs. [117,118,133–138]). Subhalos should enhance the annihilation signal, although little subhalo boost is expected in dSphs. Still, our results in this work provide conservative estimates.

In each channel of DM annihilation, the sensitivity achieves its best at $m_{\rm DM} = 630$ GeV, 1 TeV, and 250 GeV for $\bar{b}b$, W^+W^-, and $\tau^+\tau^-$, respectively. These masses are universal among the profiles. By defining the rank of the profiles with the best points of the sensitivity in the DM mass range, we examine the relation between the annihilation channel final-state spectrum and the profile. There is no change in ranks of profiles between channels. Number 14 in Table I is the strongest, Number 16 is the weakest, and all other profiles lie between them in the same order.

The dependence on the distance to the source is clarified in Fig. 4. Assuming the source of profile number 14 and number 16 at 80, 40, 160 kpc, we calculate the sensitivity and take the ratio of the upper limits on the annihilation cross section. A source distance of 80 kpc is chosen to be consistent with the distance for each model within the 1-σ error. Corresponding J-factors are shown in Table II, which shows good agreement with the scaling law of $J \propto d^{-2}$ for point sources [82,139]. The left (right) column corresponds to the profile number 14 (number 16). Profile number 14 (left) almost follows the ratio expected from the scaling of J-factors in Table II, while profile number 16 (right) does not. For profile number 16, upper limits on $\langle\sigma v\rangle$ get lower in milder ways than those expected from the scaling of the J-factor. Also, the DM mass dependence of the ratio differs between annihilation channels.

TABLE II. J-factors ($J_{\rm tot}$) of profiles number 14 and number 16 in Table I, assuming the distance from the Earth to be 40, 80, and 160 kpc.

Profile No.	$\log_{10}J_{\rm tot}$ (40 kpc)	$\log_{10}J_{\rm tot}$ (80 kpc)	$\log_{10}J_{\rm tot}$ (160 kpc)
14	19.79	19.17	18.53
16	19.18	18.58	17.98

IV. DISCUSSION

A. Dependences on profiles

The difference of $\langle\sigma v\rangle_{\rm UL}$ between profiles (short-dashed and long-dashed lines in Fig. 3, for example) is caused by two effects. Subscript "UL" denotes the upper limit here. The values of $J_{\rm tot}$ affect the sensitivity to the annihilation cross section $\langle\sigma v\rangle_{\rm UL}$ in a direct way like cases analyzing point sources with different J-factors. For analyses of extended sources, upper limits on the γ-ray flux $\phi_{\rm UL}$ are also affected by the details of DM density profiles; hence, $\langle\sigma v\rangle_{\rm UL}$ is determined by combinations of these effects. The width of the shaded regions in Fig. 3 corresponds to this fact. When sources are at large distances (e.g., $d =$ 160 kpc compared to $d = 80$ kpc), their density profile cannot be resolved. Then, the behavior of the sensitivity curve becomes like that of a point source.

To clarify this point, we show the relation between $\langle\sigma v\rangle_{\rm UL}$ and $J_{\rm tot}$ in Fig. 5. $\langle\sigma v\rangle_{\rm UL}$ is evaluated with $\langle\sigma v\rangle_{\bar{b}b}$ at $m_{\rm DM} = 630$ GeV. Each marker corresponds to a profile in Table I. The relation derived for cases of W^+W^- or $\tau^+\tau^-$ is similar. The obtained $\langle\sigma v\rangle_{\rm UL}$ does not follow the inverse of $J_{\rm tot}$, which is different from the case of $\phi_{\rm UL}$ independent of the DM distribution in dSphs like analyses of point sources. Therefore, a better understanding of the DM density profile is required in determining the goodness of the targets. We also investigate the dependence of the resultant limits on the DM density profile parameters. We search the relation between the upper limits of the annihilation cross section $\langle\sigma v\rangle$ and the DM density at a certain radius (0.1°, 0.3°, 0.5°, and 1.0°), the scale radius r_s, or the index γ defined as

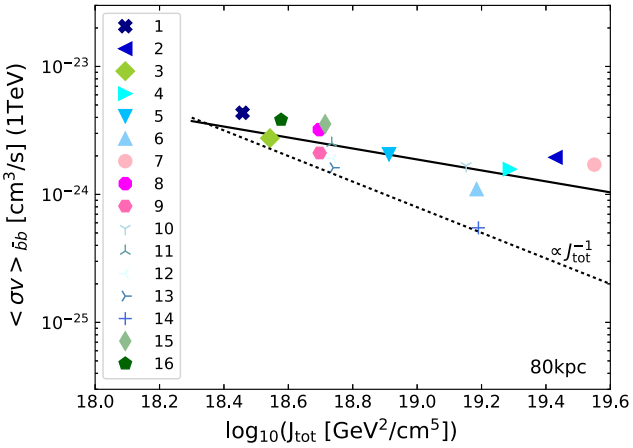

FIG. 5. Upper limits on the cross section for annihilation into $\bar{b}b$ pairs shown as a function of $J_{\rm tot}$. $\langle\sigma v\rangle_{\bar{b}b}$ is evaluated at $m_{\rm DM} = 630$ GeV. The dotted line corresponds to the relation $\langle\sigma v\rangle_{\rm UL} \propto J^{-1}$, which is expected for point sources.

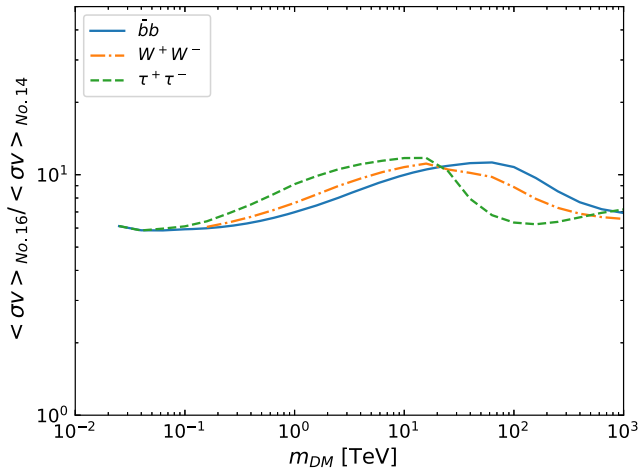

FIG. 6. Ratios of upper limits on the annihilation cross section obtained with profile number 16 and number 14 in Table I. The horizontal axis is the WIMP mass $m_{\rm DM}$, and the vertical axis is the ratio $r = \langle\sigma v\rangle_{\rm No.16}/\langle\sigma v\rangle_{\rm No.14}$. Solid, dot-dashed, and dashed lines correspond to the case considering the DM annihilating into $\bar{b}b$, W^+W^-, and $\tau^+\tau^-$, respectively.

$\rho(r) \propto r^{-\gamma}$ at the inner part ($r < r_s$). We find no correlations between either of the parameters and the achievable upper limits. Hence, none of the single profile parameters can be used to select the target dSphs, and we should select the targets based on the whole properties of their profiles.

The dependence on the DM density profile also appears in the shape of the sensitivity curve. Figure 6 shows the ratio of the obtained upper limits assuming profile number 16 and number 14 in Table I, $\langle\sigma v\rangle_{\rm No.16}/\langle\sigma v\rangle_{\rm No.14}$. For each annihilation channel, the ratio is about 10 and depends on the DM mass. A broad bump of the ratio at $m_{\rm DM} \sim 10$ to $\sim$500 TeV is seen in the case of $\bar{b}b$, while a dip at $m_{\rm DM} \sim 20$ TeV appears in the ratio for $\tau^+\tau^-$. For W^+W^-, a broad bump ranges from $\mathcal{O}(1)$ TeV to a few hundreds of tera-electron-volts, and it peaks at $m_{\rm DM} \lesssim \mathcal{O}(100)$ TeV. The DM masses at around the bumps correspond to the γ-ray emission peaks of $E_\gamma \sim 1$–10 TeV (see Fig. 2). The presence of the bumps can be interpreted as follows. The angular resolution of the CTA facility gets better as the energy increases. For example, it corresponds to about 0.1° at $E_\gamma \sim 200$ GeV and improves to about 0.04 at $E_\gamma > 1$ TeV [140]. Therefore, the changes of $\phi_{\rm UL}$ are more significant at higher energies. On the other hand, in the very-high-energy regime at $E_\gamma > 10$ TeV, almost no residual background events are expected. In such a case, the sensitivity is more determined by the detected number of signal events rather than the signal-to-noise ratio. It is a so-called signal-dominant case. In such cases, the angular resolution contributes less to the $\phi_{\rm UL}$, and $\phi_{\rm UL}$ is less affected by the spatial extension of the source. Then, $\langle\sigma v\rangle_{\rm No.16}$ can get close to the expected values for those of point sources. The behavior of the ratio $\langle\sigma v\rangle_{\rm No.16}/\langle\sigma v\rangle_{\rm No.14}$ is a manifestation of these effects since profile number 14 almost corresponds to a point source. Combining those two effects, the ratio between the profiles has the bump structures seen in Fig. 6.

B. Dependences on distances

If the same profiles of dSphs are located at different distances d_j and $d_i (> d_j)$, the J-factor increases by a factor of $(d_i/d_j)^2$ for closer ones. Then, $\langle\sigma v\rangle_{\rm UL}$ should be simply improved by $(d_i/d_j)^2$ when the target objects are point sources. However, improvements of $\langle\sigma v\rangle_{\rm UL}$ are less than those expected from the scaling of J-factors as shown in Fig. 4, due to the changes in $\phi_{\rm UL}$. Deviations from the scaling of J-factors are higher in the analyses assuming cored targets. Bumps are clearly seen in the right panels of Fig. 4. They peak at $m_{\rm DM} \lesssim \mathcal{O}(100)$ TeV for $\bar{b}b$ or W^+W^- and at $\mathcal{O}(10)$ TeV for $\tau^+\tau^-$. The features correspond to a peak at $E_\gamma \lesssim 10$ TeV in the annihilation spectrum, and a similar explanation of Sec. IV A holds. The sources at closer distances become more spatially extended such that $\phi_{\rm UL}$ gets worse at higher energies. As a result, the ratios $\langle\sigma v\rangle_{d_j}/\langle\sigma v\rangle_{d_i}$ for heavier WIMPs are more deviated from the expectations for point sources. Contributions from the noise get lower at the very-high-energy regime, and consequently at $E_\gamma > 10$ TeV, $\phi_{\rm UL}$ are less affected by the spatial sizes of the source. Combining those two effects, the ratios between the upper limits on the annihilation cross section assuming the same profiles of dSphs at different distances have the bump structures as shown in Fig. 4.

Possibilities of the uncertainties in dSph analyses due to the modelings of isotropic background events are discussed in Ref. [141]. In our analyses, the normalization of the background is fitted simultaneously with the dark matter signals; hence, the additional uncertainties due to the modelings of the background will not appear. However, the background events become Poisson-like at E_γ greater than or approximately equal to a few tera-electron-volts where we expect signals

from DM of $m_{\rm DM} \gtrsim \mathcal{O}(1)$ TeV. This might induce additional uncertainties of which contributions are small compared to those in DM spatial distributions in target dSphs. We quantify this point in future works.

V. CONCLUSION

Dependences of the accessible regions of the DM annihilation cross section $\langle \sigma v \rangle$ on the density profile of dSphs have been examined and quantified. Since the DM density profile of each dSph is still actively debated, we have taken those of Draco dSph in the literature as examples. Based on the likelihood analyses on simulated 500 hr observations with CTA assuming the 16 profiles, we have shown that the achievable upper limits on DM annihilation cross sections are highly dependent on the details of the spatial extensions of target dSphs. We have revealed that the probable region of the annihilation cross section can differ by a factor of approximately 10 if we change the profile models. The dependence is different from the case of a point source of which the merit is fully described with a single J-factor value. To extract information about the nature of DM from γ-ray observations with CTA, we therefore conclude that it is crucial to better constrain the density profiles of the targets.

The dependence of upper limits on the distance to the target dSphs have been also considered. J-factors get higher for closer targets if profiles are the same. However, achievable upper limits are always worse than those expected from the scaling of J-factors due to the larger spatial extensions of sources. This effect is significant at around γ-ray energies around 10 TeV. At around the same energy, the effect of the spatial extension of targets is also apparent in the comparison between the annihilation channels. Improved angular resolution and the signal-dominant situation in the higher γ-ray energy regions determine the behavior of the sensitivity curve in combination.

ACKNOWLEDGMENTS

We appreciate the careful reading and helpful suggestions for our earlier draft by Moritz Hütten and Vitor de Souza. Also, we thank Nicolas Produit and Subir Saker for comments. This research has made use of the CTA instrument response functions provided by the CTA Consortium and Observatory, see http://www.cta-observatory.org/science/cta-performance/ (version prod3b-v1) for more details. This work is partly supported by the JSPS KAKENHI Grant No. JP17H01131 (K. K.), and MEXT KAKENHI Grants No. JP15H05889, No. JP18H04594, JP19H05114 (K. K.), and No. JP18K03665 (M. H.). This paper has gone through internal review by the CTA consortium.

[1] L. Bergström, Nonbaryonic dark matter: Observational evidence and detection methods, Rep. Prog. Phys. **63**, 793 (2000).
[2] G. Bertone, D. Hooper, and J. Silk, Particle dark matter: Evidence, candidates and constraints, Phys. Rep. **405**, 279 (2005).
[3] J. M. Gaskins, A review of indirect searches for particle dark matter, Contemp. Phys. **57**, 496 (2016).
[4] F. Zwicky, Die Rotverschiebung von extragalaktischen Nebeln, Helv. Phys. Acta **6**, 110 (1933); Republication of: The redshift of extragalactic nebulae, Gen. Relativ. Gravit. **41**, 207 (2009).
[5] F. Zwicky, Republication of: The redshift of extragalactic nebulae, Gen. Relativ. Gravit. **41**, 207 (2009).
[6] T. S. van Albada, J. N. Bahcall, K. Begeman, and R. Sancisi, The distribution of dark matter in the spiral Galaxy NGC-3198, Astrophys. J. **295**, 305 (1985).
[7] P. Salucci and A. Borriello, The intriguing distribution of dark matter in galaxies, Lect. Notes Phys. **616**, 66 (2003).
[8] R. Barrena, A. Biviano, M. Ramella, E. E. Falco, and S. Seitz, The dynamical status of the cluster of galaxies 1e0657-56, Astron. Astrophys. **386**, 816 (2002).
[9] D. Clowe, A. Gonzalez, and M. Markevitch, Weak lensing mass reconstruction of the interacting cluster 1E0657-558: Direct evidence for the existence of dark matter, Astrophys. J. **604**, 596 (2004).
[10] P. J. E. Peebles, Large scale background temperature and mass fluctuations due to scale invariant primeval perturbations, Astrophys. J. **263**, L1 (1982).
[11] P. A. R. Ade *et al.* (Planck Collaboration), Planck 2015 results. XIII. Cosmological parameters, Astron. Astrophys. **594**, A13 (2016).
[12] E. Komatsu *et al.* (WMAP Collaboration), Seven-year Wilkinson microwave anisotropy probe (WMAP) observations: Cosmological interpretation, Astrophys. J. Suppl. Ser. **192**, 18 (2011).
[13] Y. Akrami *et al.* (Planck Collaboration), Planck 2018 results. I. Overview and the cosmological legacy of Planck, arXiv:1807.06205.
[14] N. Aghanim *et al.* (Planck Collaboration), Planck 2018 results. VI. Cosmological parameters, arXiv:1807.06209.
[15] T. Bringmann and S. Hofmann, Thermal decoupling of WIMPs from first principles, J. Cosmol. Astropart. Phys. 04 (2007) 016; Erratum 03 (2016) E02.
[16] C. Rott, Review of indirect WIMP search experiments, Nucl. Phys. B, Proc. Suppl. **235–236**, 413 (2013).
[17] R. N. Mohapatra, F. I. Olness, R. Stroynowski, and V. L. Teplitz, Searching for strongly interacting massive particles (SIMPs), Phys. Rev. D **60**, 115013 (1999).

[18] Y. Hochberg, E. Kuflik, T. Volansky, and J. G. Wacker, Mechanism for Thermal Relic Dark Matter of Strongly Interacting Massive Particles, Phys. Rev. Lett. **113**, 171301 (2014).
[19] J. Preskill, M. B. Wise, and F. Wilczek, Cosmology of the invisible axion. Phys. Lett. **120B**, 127 (1983).
[20] L. J. Rosenberg and K. A. van Bibber, Searches for invisible axions. Phys. Rep. **325**, 1 (2000).
[21] L. Visinelli and P. Gondolo, Dark matter axions revisited, Phys. Rev. D **80**, 035024 (2009).
[22] S. Dodelson and L. M. Widrow, Sterile-Neutrinos as Dark Matter, Phys. Rev. Lett. **72**, 17 (1994).
[23] X.-D. Shi and G. M. Fuller, A New Dark Matter Candidate: Nonthermal Sterile Neutrinos, Phys. Rev. Lett. **82**, 2832 (1999).
[24] K. Abazajian, G. M. Fuller, and M. Patel, Sterile neutrino hot, warm, and cold dark matter, Phys. Rev. D **64**, 023501 (2001).
[25] A. Boyarsky, O. Ruchayskiy, and M. Shaposhnikov, The role of sterile neutrinos in cosmology and astrophysics, Annu. Rev. Nucl. Part. Sci. **59**, 191 (2009).
[26] N. Afshordi, P. McDonald, and D. N. Spergel, Primordial black holes as dark matter: The power spectrum and evaporation of early structures, Astrophys. J. **594**, L71 (2003).
[27] B. Carr, F. Kuhnel, and M. Sandstad, Primordial black holes as dark matter, Phys. Rev. D **94**, 083504 (2016).
[28] B. J. Carr, K. Kohri, Y. Sendouda, and J. Yokoyama, Constraints on primordial black holes from the Galactic gamma-ray background, Phys. Rev. D **94**, 044029 (2016).
[29] B. Carr and J. Silk, Primordial black holes as seeds for cosmic structures, Mon. Not. R. Astron. Soc. **478**, 3756 (2018).
[30] K. Kohri and T. Terada, Primordial black hole dark matter and LIGO/Virgo merger rate from inflation with running spectral indices, Classical Quantum Gravity **35**, 235017 (2018).
[31] H. E. Haber and G. L. Kane, The search for supersymmetry: Probing physics beyond the Standard Model, Phys. Rep. **117**, 75 (1985).
[32] G. Jungman, M. Kamionkowski, and K. Griest, Supersymmetric dark matter, Phys. Rep. **267**, 195 (1996).
[33] J. Edsjo and P. Gondolo, Neutralino relic density including coannihilations, Phys. Rev. D **56**, 1879 (1997).
[34] J. L. Feng, K. T. Matchev, and F. Wilczek, Neutralino dark matter in focus point supersymmetry, Phys. Lett. B **482**, 388 (2000).
[35] G. F. Giudice and A. Romanino, Split supersymmetry, Nucl. Phys. **B699**, 65 (2004); Erratum, Nucl. Phys.**B706**, 487(E) (2005).
[36] G. Steigman, B. Dasgupta, and J. F. Beacom, Precise relic WIMP abundance and its impact on searches for dark matter annihilation, Phys. Rev. D **86**, 023506 (2012).
[37] M. Aaboud *et al.* (ATLAS Collaboration), Search for top-squark pair production in final states with one lepton, jets, and missing transverse momentum using 36 fb^{-1} of $\sqrt{s} =$ 13 TeV pp collision data with the ATLAS detector, J. High Energy Phys. 06 (2018) 108.
[38] A. M. Sirunyan *et al.* (CMS Collaboration), Search for dark matter produced in association with heavy-flavor quark pairs in proton-proton collisions at $\sqrt{s} = 13$ TeV, Eur. Phys. J. C **77**, 845 (2017).
[39] D. S. Akerib *et al.* (LUX Collaboration), Results from a Search for Dark Matter in the Complete LUX Exposure, Phys. Rev. Lett. **118**, 021303 (2017).
[40] C. Amole *et al.* (PICO Collaboration), Dark Matter Search Results from the PICO-60 C_3F_8 Bubble Chamber, Phys. Rev. Lett. **118**, 251301 (2017).
[41] E. Aprile *et al.* (XENON Collaboration), Dark matter search results from a one Tonne × Year exposure of XENON1T, Phys. Rev. Lett. **118**, 101101 (2017).
[42] A. Albert *et al.* (DES and Fermi-LAT Collaboration), Searching for dark matter annihilation in recently discovered Milky Way satellites with Fermi-LAT, Astrophys. J. **834**, 110 (2017).
[43] S. Tremaine and J. E. Gunn, Dynamical Role of Light Neutral Leptons in Cosmology, Phys. Rev. Lett. **42**, 407 (1979).
[44] K. Abazajian, Linear cosmological structure limits on warm dark matter, Phys. Rev. D **73**, 063513 (2006).
[45] S. Horiuchi, P. J. Humphrey, J. Onorbe, K. N. Abazajian, M. Kaplinghat, and S. Garrison-Kimmel, Sterile neutrino dark matter bounds from galaxies of the Local Group, Phys. Rev. D **89**, 025017 (2014).
[46] A. Boyarsky, J. Lesgourgues, O. Ruchayskiy, and M. Viel, Lyman-alpha constraints on warm and on warm-plus-cold dark matter models, J. Cosmol. Astropart. Phys. 05 (2009) 012.
[47] V. Verzi, D. Ivanov, and Y. Tsunesada, Measurement of energy spectrum of ultra-high energy cosmic rays, Prog. Theor. Exp. Phys. **2017**, 12A103 (2017).
[48] A. Aab *et al.* (Pierre Auger Collaboration), An indication of anisotropy in arrival directions of ultra-high-energy cosmic rays through comparison to the flux pattern of extragalactic gamma-ray sources, Astrophys. J. **853**, L29 (2018).
[49] M. G. Aartsen *et al.* (IceCube Collaboration), Neutrinos and cosmic rays observed by IceCube, Adv. Space Res. **62**, 2902 (2018).
[50] A. U. Abeysekara *et al.*, The 2HWC HAWC observatory Gamma ray catalog, Astrophys. J. **843**, 40 (2017).
[51] B. S. Acharya *et al.* (CTA Consortium Collaboration), *Science with the Cherenkov Telescope Array* (World Scientific, Singapore, 2019).
[52] M. Aguilar *et al.* (AMS Collaboration), Precision Measurement of the Proton Flux in Primary Cosmic Rays from Rigidity 1 GV to 1.8 TV with the Alpha Magnetic Spectrometer on the International Space Station. Phys. Rev. Lett. **114**, 171103 (2015).
[53] J. Chang *et al.* (DAMPE Collaboration), The Dark Matter particle explorer mission, Astropart. Phys. **95**, 6 (2017).
[54] H. Motz, Y. Asaoka, S. Torii, and S. Bhattacharyya, CALET's sensitivity to Dark Matter annihilation in the Galactic halo, J. Cosmol. Astropart. Phys. 12 (2015) 047.
[55] M. G. Aartsen *et al.* (IceCube Collaboration), Search for neutrinos from Dark Matter self-annihilations in the center of the Milky Way with 3 years of IceCube/DeepCore, Eur. Phys. J. C **77**, 627 (2017).

[56] A. Albert *et al.* (ANTARES Collaboration), Search for Dark Matter annihilation in the Earth using the ANTARES neutrino telescope, Phys. Dark Universe **16**, 41 (2017).
[57] L. Posti and A. Helmi, Mass and shape of the Milky Way's dark matter halo with globular clusters from Gaia and Hubble, Astron. Astrophys. **621**, A56 (2019).
[58] P. Gondolo and J. Silk, Dark Matter Annihilation at the Galactic Center, Phys. Rev. Lett. **83**, 1719 (1999).
[59] M. Ackermann *et al.* (Fermi-LAT Collaboration), The Fermi Galactic center GeV excess and implications for Dark Matter, Astrophys. J. **840**, 43 (2017).
[60] A. Abramowski *et al.* (H.E.S.S. Collaboration), Constraints on an Annihilation Signal from a Core of Constant Dark Matter Density around the Milky Way Center with H.E.S.S., Phys. Rev. Lett. **114**, 081301 (2015).
[61] M. Pierre, J. M. Siegal-Gaskins, and P. Scott, Sensitivity of CTA to dark matter signals from the Galactic center, J. Cosmol. Astropart. Phys. 06 (2014) 024; Erratum, J. Cosmol. Astropart. Phys.10 (2014) E01.
[62] V. Gammaldi, V. Avila-Reese, O. Valenzuela, and A. X. Gonzales-Morales, Analysis of the very inner Milky Way dark matter distribution and gamma-ray signals, Phys. Rev. D **94**, 121301 (2016).
[63] C. Taylor, M. Boylan-Kolchin, P. Torrey, M. Vogelsberger, and L. Hernquist, The mass profile of the Milky Way to the Virial radius from the illustris simulation, Mon. Not. R. Astron. Soc. **461**, 3483 (2016).
[64] G. Lake, Detectability of gamma-rays from clumps of dark matter, Nature (London) **346**, 39 (1990).
[65] N. W. Evans, F. Ferrer, and S. Sarkar, A 'Baedecker' for the dark matter annihilation signal, Phys. Rev. D **69**, 123501 (2004).
[66] N. F. Martin *et al.*, Hydra II: A faint and compact Milky Way Dwarf Galaxy found in the survey of the magellanic stellar history, Astrophys. J. **804**, L5 (2015).
[67] D. Kim and H. Jerjen, Horologium II: A second ultra-faint Milky Way satellite in the horologium constellation, Astrophys. J. **808**, L39 (2015).
[68] B. P. M. Laevens *et al.*, A new faint Milky Way satellite discovered in the Pan-STARRS1 3 pi survey, Astrophys. J. **802**, L18 (2015).
[69] B. P. M. Laevens *et al.*, Sagittarius II, Draco II and Laevens 3: Three new Milky way satellites discovered in the Pan-starrs 1 3π survey, Astrophys. J. **813**, 44 (2015).
[70] E. Luque *et al.* (DES Collaboration), Digging deeper into the southern skies: A compact Milky-Way companion discovered in first-year Dark Energy survey data, Mon. Not. R. Astron. Soc. **458**, 603 (2016).
[71] S. E. Koposov *et al.*, Kinematics and chemistry of recently discovered Reticulum 2 and Horologium 1 Dwarf Galaxies, Astrophys. J. **811**, 62 (2015).
[72] K. Bechtol *et al.* (DES Collaboration), Eight new Milky Way companions discovered in first-year Dark Energy survey data, Astrophys. J. **807**, 50 (2015).
[73] A. W. McConnachie, The observed properties of Dwarf Galaxies in and around the local group, Astron. J. **144**, 4 (2012).
[74] (Gaia Collaboration), Gaia data release 2. Kinematics of globular clusters and Dwarf Galaxies around the Milky Way, Astron. Astrophys. **616**, A12 (2018).
[75] J. D. Simon, Gaia proper motions and orbits of the ultra-faint Milky Way satellites, Astrophys. J. **863**, 89 (2018).
[76] L. E. Strigari, S. M. Koushiappas, J. S. Bullock, and M. Kaplinghat, Precise constraints on the dark matter content of Milky Way Dwarf Galaxies for gamma-ray experiments, Phys. Rev. D **75**, 083526 (2007).
[77] A. Charbonnier *et al.*, Dark matter profiles and annihilation in Dwarf spheroidal galaxies: Prospectives for present and future gamma-ray observatories—I. The classical dSphs, Mon. Not. R. Astron. Soc. **418**, 1526 (2011).
[78] K. Hayashi, K. Ichikawa, S. Matsumoto, M. Ibe, M. N. Ishigaki, and H. Sugai, Dark matter annihilation and decay from non-spherical dark halos in galactic Dwarf satellites, Mon. Not. R. Astron. Soc. **461**, 2914 (2016).
[79] M. Mateo, Dwarf galaxies of the local group, Annu. Rev. Astron. Astrophys. **36**, 435 (1998).
[80] L. E. Strigari, S. M. Koushiappas, J. S. Bullock, M. Kaplinghat, J. D. Simon, M. Geha, and B. Willman, The most Dark Matter dominated Galaxies: Predicted Gamma-ray signals from the faintest Milky Way Dwarfs, Astrophys. J. **678**, 614 (2008).
[81] G. Battaglia, A. Helmi, and M. Breddels, Internal kinematics and dynamical models of Dwarf spheroidal galaxies around the Milky Way, New Astron. Rev. **57**, 52 (2013).
[82] A. B. Pace and L. E. Strigari, Scaling relations for Dark Matter annihilation and decay profiles in Dwarf spheroidal Galaxies, Mon. Not. R. Astron. Soc. **482**, 3480 (2019).
[83] M. Irwin and D. Hatzidimitriou, Structural parameters for the Galactic Dwarf spheroidals, Mon. Not. R. Astron. Soc. **277**, 1354 (1995).
[84] A. Geringer-Sameth, M. G. Walker, S. M. Koushiappas, S. E. Koposov, V. Belokurov, G. Torrealba, and N. W. Evans, Indication of Gamma-ray Emission from the Newly Discovered Dwarf Galaxy Reticulum II, Phys. Rev. Lett. **115**, 081101 (2015).
[85] A. A. Abdo *et al.* (Fermi-LAT Collaboration), Observations of Milky Way Dwarf spheroidal galaxies with the Fermi-LAT detector and constraints on Dark Matter models, Astrophys. J. **712**, 147 (2010).
[86] M. Ackermann *et al.* (Fermi-LAT Collaboration), Constraining Dark Matter Models from a Combined Analysis of Milky Way Satellites with the Fermi Large Area Telescope, Phys. Rev. Lett. **107**, 241302 (2011).
[87] M. Ackermann *et al.* (Fermi-LAT Collaboration), Dark matter constraints from observations of 25 Milky Way satellite galaxies with the Fermi Large Area Telescope, Phys. Rev. D **89**, 042001 (2014).
[88] M. Ackermann *et al.* (Fermi-LAT Collaboration), Searching for Dark Matter Annihilation from Milky Way Dwarf Spheroidal Galaxies with Six Years of Fermi Large Area Telescope Data, Phys. Rev. Lett. **115**, 231301 (2015).
[89] E. Charles *et al.* (Fermi-LAT Collaboration), Sensitivity projections for Dark Matter searches with the Fermi large area telescope, Phys. Rep. **636**, 1 (2016).
[90] J. Aleksic *et al.* (MAGIC Collaboration), Searches for Dark Matter annihilation signatures in the Segue 1 satellite galaxy with the MAGIC-I telescope, J. Cosmol. Astropart. Phys. 06 (2011) 035.

[91] J. Aleksić *et al.*, Optimized dark matter searches in deep observations of Segue 1 with MAGIC, J. Cosmol. Astropart. Phys. 02 (2014) 008.
[92] M. Doro (MAGIC Collaboration), A review of the past and present MAGIC dark matter search program and a glimpse at the future, in *25th European Cosmic Ray Symposium (ECRS 2016) Turin, Italy, 2016* (2017), https://inspirehep.net/record/1510040/files/arXiv:1701.05702.pdf.
[93] M. L. Ahnen *et al.* (MAGIC Collaboration), Indirect dark matter searches in the Dwarf satellite galaxy Ursa major II with the MAGIC telescopes, J. Cosmol. Astropart. Phys. 03 (2018) 009.
[94] F. Aharonian (H.E.S.S. Collaboration), Observations of the sagittarius Dwarf Galaxy by the H.E.S.S. experiment and search for a Dark Matter signal, Astropart. Phys. **29**, 55 (2008); Erratum, Astropart. Phys. **33**, 274(E) (2010).
[95] F. Aharonian (H.E.S.S. Collaboration), A search for a dark matter annihilation signal towards the Canis Major overdensity with H.E.S.S, Astrophys. J. **691**, 175 (2009).
[96] A. Abramowski *et al.* (H.E.S.S. Collaboration), H.E.S.S. constraints on Dark Matter annihilations towards the Sculptor and Carina Dwarf Galaxies, Astropart. Phys. **34**, 608 (2011).
[97] A. Abramowski *et al.* (H.E.S.S. Collaboration), Search for dark matter annihilation signatures in H.E.S.S. observations of Dwarf Spheroidal Galaxies, Phys. Rev. D **90**, 112012 (2014).
[98] V. A. Acciari *et al.* (VERITAS Collaboration), VERITAS Search for VHE Gamma-ray emission from Dwarf spheroidal Galaxies, Astrophys. J. **720**, 1174 (2010).
[99] E. Aliu *et al.* (VERITAS Collaboration), VERITAS deep observations of the Dwarf spheroidal Galaxy segue 1, Phys. Rev. D **85**, 062001 (2012); Erratum, Phys. Rev. D**91**, 129903(E) (2015).
[100] S. Archambault *et al.* (VERITAS Collaboration), Dark Matter constraints from a joint analysis of Dwarf spheroidal Galaxy observations with VERITAS, Phys. Rev. D **95**, 082001 (2017).
[101] A. Albert *et al.* (HAWC Collaboration), Dark Matter limits from Dwarf spheroidal Galaxies with The HAWC Gamma-ray observatory, Astrophys. J. **853**, 154 (2018).
[102] R. Essig, N. Sehgal, L. E. Strigari, M. Geha, and J. D. Simon, Indirect dark matter detection limits from the ultrafaint Milky Way satellite segue 1, Phys. Rev. D **82**, 123503 (2010).
[103] M. L. Ahnen *et al.* (Fermi-LAT and MAGIC Collaboration), Limits to dark matter annihilation cross-section from a combined analysis of MAGIC and Fermi-LAT observations of dwarf satellite galaxies, J. Cosmol. Astropart. Phys. 02 (2016) 039.
[104] L. Ambrogi, S. Celli, and F. Aharonian, On the potential of Cherenkov telescope arrays and KM3 neutrino telescopes for the detection of extended sources, Astropart. Phys. **100**, 69 (2018).
[105] V. Bonnivard, D. Maurin, and M. G. Walker, Contamination of stellar-kinematic samples and uncertainty about dark matter annihilation profiles in ultrafaint dwarf galaxies: The example of Segue I, Mon. Not. R. Astron. Soc. **462**, 223 (2016).
[106] S. Mashchenko, A. Sills, and H. M. P. Couchman, Constraining global properties of the draco dwarf spheroidal galaxy, Astrophys. J. **640**, 252 (2006).
[107] M. A. Sanchez-Conde, F. Prada, E. L. Lokas, M. E. Gomez, R. Wojtak, and M. Moles, Dark Matter annihilation in Draco: New considerations of the expected gamma flux, Phys. Rev. D **76**, 123509 (2007).
[108] A. Geringer-Sameth, S. M. Koushiappas, and M. Walker, Dwarf galaxy annihilation and decay emission profiles for dark matter experiments, Astrophys. J. **801**, 74 (2015).
[109] E. L. Lokas, Dark matter distribution in dwarf spheroidal galaxies, Mon. Not. R. Astron. Soc. **333**, 697 (2002).
[110] E. L. Lokas, G. A. Mamon, and F. Prada, Dark matter distribution in the Draco dwarf from velocity moments, Mon. Not. R. Astron. Soc. **363**, 918 (2005).
[111] J. Knödlseder *et al.*, GammaLib and ctools: A software framework for the analysis of astronomical gamma-ray data, Astron. Astrophys. **593**, A1 (2016).
[112] L. Hernquist, An analytical model for spherical Galaxies and bulges. Astrophys. J. **356**, 359 (1990).
[113] H. Zhao, Analytical models for galactic nuclei, Mon. Not. R. Astron. Soc. **278**, 488 (1996).
[114] J. F. Navarro, C. S. Frenk, and S. D. M. White, A Universal density profile from hierarchical clustering, Astrophys. J. **490**, 493 (1997).
[115] A. Burkert, The structure of dark matter halos in dwarf galaxies, IAU Symp. **171** (1996) 175; Astrophys. J. **447**, L25 (1995).
[116] V. Bonnivard, C. Combet, D. Maurin, and M. G. Walker, Spherical Jeans analysis for dark matter indirect detection in dwarf spheroidal galaxies—Impact of physical parameters and triaxiality, Mon. Not. R. Astron. Soc. **446**, 3002 (2015).
[117] V. Bonnivard, M. Hütten, E. Nezri, A. Charbonnier, C. Combet, and D. Maurin, CLUMPY: Jeans analysis, γ-ray and ν fluxes from dark matter (sub-)structures, Comput. Phys. Commun. **200**, 336 (2016).
[118] M. Hütten, C. Combet, G. Maier, and D. Maurin, Dark matter substructure modelling and sensitivity of the Cherenkov telescope array to Galactic dark halos, J. Cosmol. Astropart. Phys. 09 (2016) 047.
[119] T. Sjöstrand, S. Ask, J. R. Christiansen, R. Corke, N. Desai, P. Ilten, S. Mrenna, S. Prestel, C. O. Rasmussen, and P. Z. Skands, An introduction to PYTHIA 8.2, Comput. Phys. Commun. **191**, 159 (2015).
[120] T. Sjostrand, S. Mrenna, and P. Z. Skands, PYTHIA 6.4 physics and manual, J. High Energy Phys. 05 (2006) 026.
[121] T. Sjostrand, S. Mrenna, and P. Z. Skands, A brief introduction to PYTHIA 8.1, Comput. Phys. Commun. **178**, 852 (2008).
[122] A. V. Belikov and D. Hooper, The contribution of inverse Compton scattering to the diffuse extragalactic Gamma-ray background from annihilating Dark Matter, Phys. Rev. D **81**, 043505 (2010).
[123] M. Cirelli and P. Panci, Inverse Compton constraints on the dark matter $e+e-$ excesses, Nucl. Phys. **B821**, 399 (2009).
[124] S. Profumo and T. E. Jeltema, Extragalactic inverse Compton light from dark matter annihilation and the Pamela positron excess, J. Cosmol. Astropart. Phys. 07 (2009) 020.

[125] C. Blanco, J. P. Harding, and D. Hooper, Novel Gamma-ray signatures of PeV-scale dark matter, J. Cosmol. Astropart. Phys. 04 (2018) 060.
[126] R. Bartels, D. Gaggero, and C. Weniger, Prospects for indirect dark matter searches with MeV photons, J. Cosmol. Astropart. Phys. 05 (**2017**) 001.
[127] M. Cirelli, G. Corcella, A. Hektor, G. Hutsi, M. Kadastik, P. Panci, M. Raidal, F. Sala, and A. Strumia, PPPC 4 DM ID: A poor particle physicist cookbook for dark matter indirect detection, J. Cosmol. Astropart. Phys. 03 (2011) 051; Erratum, J. Cosmol. Astropart. Phys.10 (2012) E01.
[128] P. Cumani, T. Hassan, L. Arrabito, K. Bernlöhr, J. Bregeon, G. Maier, and A. Moralejo (CTA Consortium Collaboration), Baseline telescope layouts of the Cherenkov telescope array, Proc. Sci., ICRC2017 (**2018**) 811.
[129] H. Abdalla *et al.* (HESS Collaboration), Searches for gamma-ray lines and "pure WIMP" spectra from Dark Matter annihilations in dwarf galaxies with H.E.S.S, J. Cosmol. Astropart. Phys. 11 (**2018**) 037.
[130] M. Wood, J. Buckley, S. Digel, S. Funk, D. Nieto, and M. A. Sanchez-Conde, Prospects for indirect detection of Dark Matter with CTA, in *Proceedings, 2013 Community Summer Study on the Future of U.S. Particle Physics: Snowmass on the Mississippi (CSS2013): Minneapolis, MN, USA, 2013* (PUBLISHER, LOCATION, 2013), http://www.slac.stanford.edu/econf/C1307292/docs/submittedArxivFiles/1305.0302.pdf.
[131] H. Silverwood, C. Weniger, P. Scott, and G. Bertone, A realistic assessment of the CTA sensitivity to dark matter annihilation, J. Cosmol. Astropart. Phys. 03 (2015) 055.
[132] L. Roszkowski, E. M. Sessolo, and A. J. Williams, Prospects for dark matter searches in the pMSSM, J. High Energy Phys. 02 (2015) 014.
[133] M. A. Sanchez-Conde and F. Prada, The flattening of the concentration-mass relation towards low halo masses and its implications for the annihilation signal boost, Mon. Not. R. Astron. Soc. **442**, 2271 (2014).
[134] A. Moline, M. A. Sanchez-Conde, S. Palomares-Ruiz, and F. Prada, Characterization of subhalo structural properties and implications for dark matter annihilation signals, Mon. Not. R. Astron. Soc. **466**, 4974 (2017).
[135] M. Stref and J. Lavalle, Modeling dark matter subhalos in a constrained galaxy: Global mass and boosted annihilation profiles, Phys. Rev. D **95**, 063003 (2017).
[136] N. Hiroshima, S. Ando, and T. Ishiyama, Modeling evolution of dark matter substructure and annihilation boost, Phys. Rev. D **97**, 123002 (2018).
[137] A. Charbonnier, C. Combet, and D. Maurin, CLUMPY: A code for gamma-ray signals from dark matter structures, Comput. Phys. Commun. **183**, 656 (2012).
[138] M. Hutten, C. Combet, and D. Maurin, CLUMPY v3: γ-ray and ν signals from dark matter at all scales, Comput. Phys. Commun. **235**, 336 (2019).
[139] N. W. Evans, J. L. Sanders, and A. Geringer-Sameth, Simple J-factors and D-factors for indirect dark matter detection, Phys. Rev. D **93**, 103512 (2016).
[140] T. Hassan *et al.*, Monte Carlo performance studies for the site selection of the Cherenkov telescope array, Astropart. Phys. **93**, 76 (2017).
[141] F. Calore, P. D. Serpico, and B. Zaldivar, Dark matter constraints from dwarf galaxies: A data-driven analysis, J. Cosmol. Astropart. Phys. 10 (2018) 029.